Understanding interfacial behavior of materials via *in situ* micromechanical characterization

Siyang Wang,* Rui Hao, Soumyajit Mojumder, Henri Nela, Phoebe Rylatt, Zonghao Shen, Finn Giuliani,* and Oriol Gavalda-Diaz*

We present here a series of examples demonstrating how *in situ* electron microscopy micromechanical characterization can be employed to understand the behavior of individual interfaces that often dictate macroscale mechanical performance. We highlight how careful experimental design enables characterization of targeted interfaces under application-relevant loading conditions, thereby revealing critical mechanical properties and failure mechanisms. To achieve this, we show exemplary testing geometries for studying various deformation and fracture modes in materials relevant to nuclear, aerospace, and energy storage applications. We also propose testing and characterization strategies that may advance the understanding of interfacial failure in functional devices. Taken together, we hope to inspire wider application of these *in situ* micromechanical approaches as well as the development of novel methodologies for improved scientific insights.

Impact statement

Interfaces, the boundaries between dissimilar domains within materials, often control damage initiation and propagation during mechanical failure. The usually complex microstructure of engineering materials means that mechanical testing of the material as a whole provides only the overall mechanical response but makes it difficult to determine the contributions of individual interfaces. Motivated by this, we present a range of examples to illustrate how *in situ* micromechanical characterization within scanning and transmission electron microscopes (SEM and TEM) can address this knowledge gap. This approach involves mechanically testing micron- or submicron-scale specimens, typically fabricated by focused ion beam milling, that contain only one or a few interfaces, while directly observing how the tested interface(s) fail and measuring their micromechanical properties. Using *in situ* approaches, we can achieve well-defined loading conditions that facilitate data interpretation and access the dynamic evolution of the failure mechanisms. Our examples span diverse material systems and failure modes relevant to real-world applications, which include ductile deformation, brittle fracture, and environmental-assisted failure of individual interfaces. We also discuss how in situ micromechanical characterisation may be further developed to enable broader applications and deeper insights.

Introduction

The critical role of interfaces in the mechanical performance of materials has long been recognized. Typical examples include the control of deformation and fracture by grain and phase boundaries in metals and ceramics, the load transfer or crack deflection of interfaces in fiber composites, and the deterioration of mechanical properties by undesirable interfaces formed through material–environment interactions. Macroscale mechanical testing provides quantitative measurements of the overall mechanical response of materials and, particularly for engineering components, enables material behavior to be evaluated at length scales relevant to practical applications, thereby directly informing engineering practice. It is often combined with post-mortem characterization to reveal the resultant damage structures within materials, from which the underlying failure mechanisms can be inferred.

There are, however, critical information that can be difficult to obtain using the above approach, particularly.

(a) The mechanical properties and behavior of individual interfaces;
(b) The contributions of individual interfaces to the overall performance of materials (e.g., through multiscale models);
(c) The detailed path through which interfaces degrade or fail.

The lack of such data and knowledge would restrict the development of physics-based models that can assist the understanding and prediction of the mechanical performance

Siyang Wang, Department of Materials, Royal School of Mines, Imperial College London, London SW7 2AZ, UK; siyang.wang15@imperial.ac.uk
Rui Hao, Department of Materials, Royal School of Mines, Imperial College London, London SW7 2AZ, UK
Soumyajit Mojumder, Department of Materials, Royal School of Mines, Imperial College London, London SW7 2AZ, UK
Henri Nela, Department of Materials, Royal School of Mines, Imperial College London, London SW7 2AZ, UK
Phoebe Rylatt, Department of Materials, Royal School of Mines, Imperial College London, London SW7 2AZ, UK
Zonghao Shen, Imperial Global Singapore (IGS), Imperial College London, 1 CREATE Way, #11-01, CREATE Tower, Singapore 138602, Singapore
Finn Giuliani, Department of Materials, Royal School of Mines, Imperial College London, London SW7 2AZ, UK; Imperial Global Singapore (IGS), Imperial College London, 1 CREATE Way, #11-01, CREATE Tower, Singapore 138602, Singapore; f.giuliani@imperial.ac.uk
Oriol Gavalda-Diaz, Department of Materials, Royal School of Mines, Imperial College London, London SW7 2AZ, UK; o.gavalda-diaz@imperial.ac.uk
*Corresponding author
doi:10.1557/s43577-026-01234-4

© The Author(s) 2026

of materials in real applications. *In situ* micromechanical characterization[1,2] has been an effective attempt to address these limitations. Through testing small-scale specimens that contain only targeted interfaces, often fabricated site-specifically via focused ion beam (FIB) milling, the stress state at interfaces can be significantly simplified compared to macroscale tests, thereby allowing interfacial properties to be determined. Performing the tests *in situ,* inside an SEM or a TEM, also enables both precise control of the applied load, usually using an indenter tip, and (near) real-time, high-resolution visualization of the failure processes. In addition, the flexibility that current FIB systems provide together with experimental designs can enable the realization of various specimen and testing geometries, thereby the extraction of the micromechanical properties is most relevant to the materials' intended applications.

The practical implementation of such characterisation also involves several important considerations, for example.

(1) The sample preparation and testing processes can be technically involved and therefore time-consuming, which might limit statistical sampling;
(2) Bespoke indenter tips required for specific testing geometries may be difficult to acquire or prepare;
(3) Testing geometries and methodologies, including the shape, dimensions, and aspect ratio of test pieces, as well as the loading rate and imaging protocols, are not yet fully standardized;
(4) Characterization using electron microscopy, particularly SEM, is, strictly speaking, only near real time due to the (typically ~1 s) time required to acquire images with sufficient spatial resolution and signal-to-noise ratio. Hence, the imaging conditions must be determined for each experiment in line with the applied displacement rate and the expected timescale of the mechanical processes of interest.

In this work, we present a range of examples spanning various material systems, interface types, and testing geometries, to showcase how micromechanical testing, coupled with *in situ* characterization with SEM or TEM, can uncover useful insights into the underlying mechanisms governing interfacial failure. These are summarized in the graphical abstract and discussed in more detail below. We should note that this work is not intended to be a thorough review of the studies in this field, but a perspective from the authors that is supported using original research outcomes of our own. The aim of this brief perspective is to highlight the range of techniques that are available to characterize interfaces in different materials. Because most of these techniques have published before by us or other groups, we do not use this perspective to detail the analysis process but rather to direct the reader to the relevant literature. The particular focus of this work is on the behavior of individual interfaces; studies involving multiple interfaces, such as nanolaminates and multilayers, have been reported elsewhere (e.g., References 3–7).

Deformation

We start with examples of ductile deformation at interfaces. Al_2O_3–Nb is a widely studied model ceramic–metal system due to (1) their closely matched coefficients of thermal expansion, (2) the small mismatch between their lattice parameters for a number of crystal orientations, and (3) the absence of chemical reactions at their interface when bonded in vacuum. The micropillars presented in **Figure 1**a were fabricated in samples polished such that the Nb interlayers are inclined at ~45° to the surfaces, so as to place the interlayer on the plane of maximum shear and hence promote interfacial sliding during a pillar compression test. While the pillar containing a 60-nm-thick interlayer exhibited a stress drop shortly after yielding consistent with brittle failure, the pillars containing 120- and 240-nm-thick interlayers showed a distinct behavior. They both experienced noticeable plastic flow, suggesting that interfacial sliding is increasingly accommodated by plastic deformation of the Nb interlayer as its thickness increases. An inverse relationship between the yield strength and interlayer thickness can also be observed, which is likely associated with the reduced confinement of plastic deformation in thicker Nb layers and/or a thickness-dependent size effect arising from the limited availability of dislocation sources in the thinner interlayers. Post-mortem TEM examination of the Al_2O_3–Nb interfaces in the deformed pillars (representative data shown in Figure 1b) provided further insight into their atomic-scale structure following deformation, as well as the orientation relationship (OR) between the two phases. For the diffraction patterns shown, which were obtained from a Nb grain and the adjacent Al_2O_3 region at the bottom interface, the OR was found to be $(0001)_{Al_2O_3}||(110)_{Nb}$, $\langle 11\bar{2}0\rangle_{Al_2O_3}||\langle 1\bar{1}2\rangle_{Nb}$, $\langle 1\bar{1}00\rangle_{Al_2O_3}||\langle \bar{1}11\rangle_{Nb}$).

The same approach of studying interfacial failure has been applied to "sandwich" structures in other material systems such as hydrides in zirconium. The mechanical behavior of the Zr–H system is industrially important, as Zr alloys are used as fuel cladding in nuclear reactors where reactions with the surrounding coolant water can cause hydrogen embrittlement of the cladding.[9] Figure 1c shows the deformation process of a Zircaloy-4 (a type of Zr alloy) micropillar that contains a Zr hydride plate inclined at ~45° to the loading axis, where deformation is highly localized at the hydride–metal interface. In the absence of hydrides, deformation for this specific crystallographic configuration is typically accommodated by basal slip, of which the character is broad/diffuse.[8] This is deemed an embrittling mechanism, as localized shear is a well-known precursor to rupture in metallic materials.[10]

Apart from interfacial shear/sliding, appropriate experimental design can also allow the study of slip transmission across interfaces. In Figure 1d, the same material as (c) was studied, but this time with a hydride plate sitting nearly

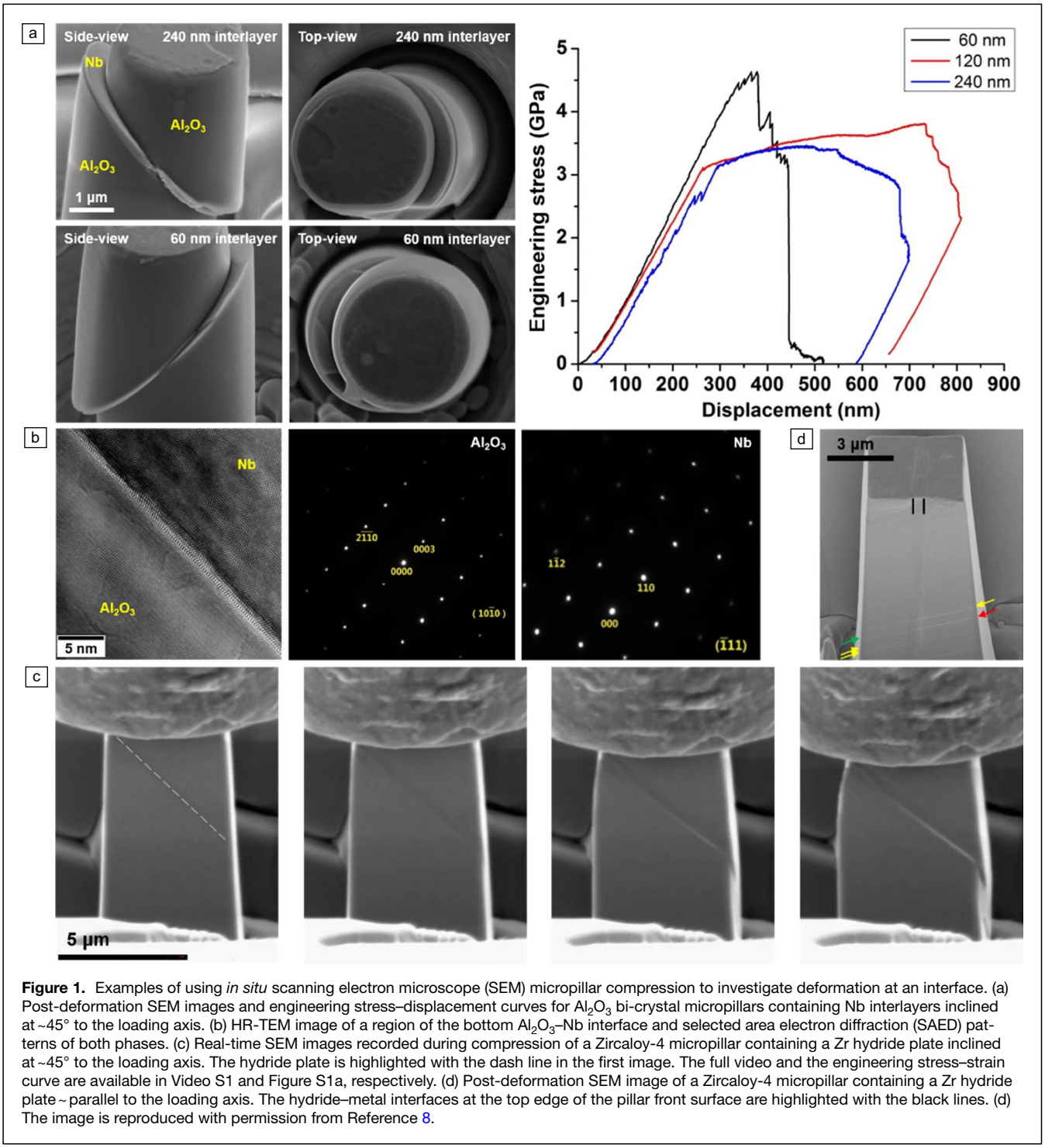


Figure 1. Examples of using *in situ* scanning electron microscope (SEM) micropillar compression to investigate deformation at an interface. (a) Post-deformation SEM images and engineering stress–displacement curves for Al_2O_3 bi-crystal micropillars containing Nb interlayers inclined at ~45° to the loading axis. (b) HR-TEM image of a region of the bottom Al_2O_3–Nb interface and selected area electron diffraction (SAED) patterns of both phases. (c) Real-time SEM images recorded during compression of a Zircaloy-4 micropillar containing a Zr hydride plate inclined at ~45° to the loading axis. The hydride plate is highlighted with the dash line in the first image. The full video and the engineering stress–strain curve are available in Video S1 and Figure S1a, respectively. (d) Post-deformation SEM image of a Zircaloy-4 micropillar containing a Zr hydride plate ~ parallel to the loading axis. The hydride–metal interfaces at the top edge of the pillar front surface are highlighted with the black lines. (d) The image is reproduced with permission from Reference 8.

vertically in the middle of the pillar. Slip bands initiated in the soft metal phase, and, in most cases, were blocked at the hydride–metal interfaces (those highlighted with the yellow arrows). One slip band (marked with the green arrow) propagated through the hydride and triggered slip on the other side of the hydride (marked with the red arrow). Such blocked slip bands may lead to local stress concentrations and later microvoids, and this could be a second embrittling mechanism. Other applications of micropillar testing in understanding deformation at interfaces can be found in Reference 11, for example, alongside the employment of other testing geometries such as microcantilever[12] and micro-tensile[13] testing.

Fracture

FIB-milled notches make it possible to perform fracture tests on microscale specimens and measure the fracture toughness of specific interfaces. A key limitation for brittle materials is that these tests produce unstable cracks, so toughness values can only be extracted at the moment a crack initiates from the FIB-milled notch. This approach has drawbacks, since ion implantation during FIB milling can cause amorphisation and residual stress build-up. Several strategies exist to overcome this limitation (see for instance References 14–16); here, we focus on microscale double cantilever beam (DCB) tests for evaluating the properties of individual interfaces. **Figure 2**a shows the images recorded during a microscale DCB splitting test, similar to the classic design described by Obreimoff,[17] with the interface placed vertical. During such a test, the real-time stored elastic strain energy in the cantilever beams can be calculated from the deflections of the beams and the length of the crack based on a linear elasticity assumption. As the crack propagates along the interface, the released strain energy is assumed to be fully dissipated through crack growth, thereby allowing the determination of the fracture energy. As such, fracture energy can be extracted using the SEM images recorded alone without the need for load–displacement data. Full details about the data analysis procedure for DCB tests can be found in Reference 14. When conducted in (real) displacement control, the driving force decreases with crack length, thus stable crack growth can be achieved. In geometries other than DCB where there is stable crack growth, crack propagation is usually significantly faster than the acquisition speed of electron microscopes, meaning that even with *in situ* testing, the analysis can be post-mortem and critical failure points and mechanisms may be missed. Therefore, DCB testing can be useful when mechanistic results are required. This methodology has also been extended to *in situ* TEM characterisation (an image of the samples is presented in Figure 2b), where benefits include higher-resolution visualisation, nano-diffraction strain mapping,[18] and capturing local phase transformations near the crack tip.[19] Figure 2c shows the images recorded during an *in situ* TEM test of a DCB sample fabricated with the notch plane along the fiber-matrix C interphase in a SiC/SiC ceramic matrix composite (CMC), a promising candidate material for next-generation aeroengines and nuclear reactors.[20] In this specific interphase, the crack is observed to propagate within the C interphase. However, this testing geometry opens the possibility to test different interphases and understand how interphase microstructure affects the crack deflection in CMCs and more globally in composites.

Crack deflection and other toughening mechanisms in fiber composites are governed by mixed-mode fracture behavior,[21] and therefore, the determination of fracture properties under different loading modes is crucial for predicting macroscale performance. While the Mode I interfacial fracture energy can be measured through DCB testing, fiber push-out (Figure 2d) and push-in[22,23] testing provides access to mode II (sliding) fracture behavior. For push-out tests, key measurable properties include the interfacial shear strength,[24] the interfacial friction,[25] and the mode II fracture energy.[25,26] To ensure successful push-out, the critical interfacial rupture force must not exceed either the critical load for fiber interior fracture or the load limit of the test rig. This requires the sample thickness, and therefore the fiber length, to be sufficiently small. Where controlled mechanical polishing to micron-scale thicknesses is challenging, this can instead be achieved by micromachining trenches a short distance below the surface using techniques such as FIB milling[27] or femtosecond laser processing[28] and subsequently push the fibers into the trenches (Figure 2d). The load–displacement curve for this test, shown in Figure S1b, exhibits several characteristic stages, including elastic deformation, progressive interfacial debonding, fiber push-out, and interfacial sliding, each distinguished by a distinct mechanical response. An additional advantage of this FIB-assisted microscale push-out approach is that it enables testing of small-volume samples. This is particularly important when studying the effects of irradiation on the mechanical properties of fiber composites for nuclear reactors, as ion implantation experiments often produce only limited irradiated volumes.[29]

Non-structural materials

One should note that mechanical degradation is not a phenomenon only found in structural materials. Degradation of functional materials is frequently observed to occur through various mechanisms such as chemical intercalation,[30] phase transformation,[31] and magnetic phase transition,[32] hence, understanding their mechanical properties and degradation mechanisms is vital for predicting failure and developing strategies to extend lifetime. The past few years have seen a growing popularity in using *in situ* micromechanical characterization to study interfacial failure in functional materials. **Figure 3**a presents the failure process of a pristine (not electrochemically cycled) polycrystalline $Li(Ni_{0.8}Mn_{0.1}Co_{0.1})O_2$ (NMC811) secondary particle under compression, where cracks are observed to develop along grain boundaries of the primary particles. This material is one of the major cathode materials used in current-generation Li-ion batteries, yet its gradual degradation contributes to capacity loss of batteries over long-term cycling, with cracking of the high-Ni electrode particles commonly observed. Compression testing serves as a straightforward approach to measure particle strength as well as its evolution with charge–discharge cycling.[30] Better-defined sample geometries, such as micropillars (Figure 3b, which illustrates a grain-boundary shear fracture event in sintered NMC811) and microcantilevers,[33] require sometimes sophisticated preparation with FIB machining but provide advantages in (1) well-established load–stress relationships, hence confident determination of material properties, and (2) testing of targeted interfaces.

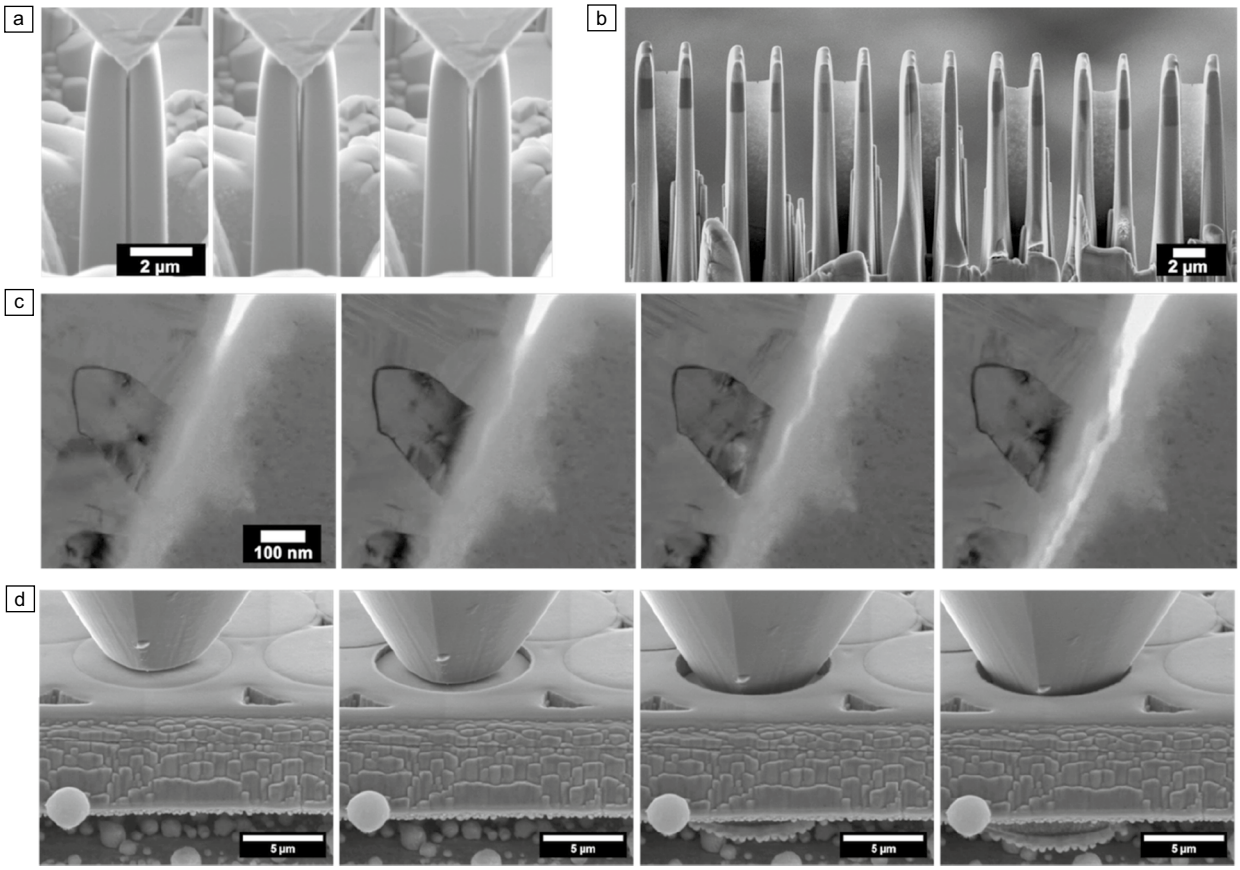


Figure 2. Examples of using *in situ* scanning electron microscope (SEM) and transmission electron microscope (TEM) micromechanical characterization to investigate fracture at an interface. (a) Real-time SEM images recorded during splitting of a double cantilever beam (DCB) sample fabricated with the notch plane along the fiber-matrix BN interphase in a SiC/SiC ceramic matrix composite (CMC).[20] The full video is available in Video S2. (b) SEM image showing an array of thin-foil DCB samples for *in situ* TEM testing. (c) Real-time TEM images recorded during splitting of a DCB sample fabricated with the notch plane along the fiber-matrix C interphase in a SiC/SiC CMC. The full video is available in Video S3. (d) Real-time SEM images recorded during push-out of a SiC fiber in a SiC/SiC CMC. The trench underneath the tested fiber was produced via FIB milling. The full video and the load–displacement curve are available in Video S4 and Figure S1b, respectively.

To summarize, we have presented a few examples illustrating how *in situ* SEM and TEM micromechanical characterization can be used to understand the microscale interfacial behavior of materials for a wide range of applications. We showed how experimental strategies can be tailored to reveal interfacial properties of scientific importance and industrial relevance for each application. In this regard, an important direction in this field is the continued development of *operando* approaches that subject functional materials to service-relevant stimuli (e.g., electrochemical and magnetic cycling) while retaining the ability to observe individual interfaces, thereby enabling more directly relevant insights into their failure mechanisms. In addition, high-temperature micromechanical testing of individual interfaces would provide insights into the interfacial behavior of materials at service temperatures in applications such as aerospace and nuclear. Further integrating these approaches with advanced characterization techniques, such as high-angular-resolution electron backscatter diffraction (HR-EBSD), high-spatial-resolution digital image correlation (HR-DIC),[34] and four-dimensional scanning transmission electron microscopy (4D-STEM), offers the potential to map local stress, strain, and geometrically necessary dislocation density distributions near critical interfaces, providing deeper insights into their role in materials performance.

Materials and methods

The Nb interlayers within Al_2O_3 bi-crystals were prepared through first depositing Nb on the surface of the *c*-plane (0001) Al_2O_3 through magnetron sputtering at 400°C, followed by diffusion bonding two coated Al_2O_3 crystals (with the $< 10\bar{1}0 >$ and $< 11\bar{2}0 >$ orientations aligned and the Nb layers in between) at 1600°C in a hot press furnace, under a pressure of 30 MPa and in a vacuum of less than 10^{-5} Torr.

The hydride-containing Zircaloy-4 sample was fabricated through first electrolytically hydrogen charging Zircaloy-4

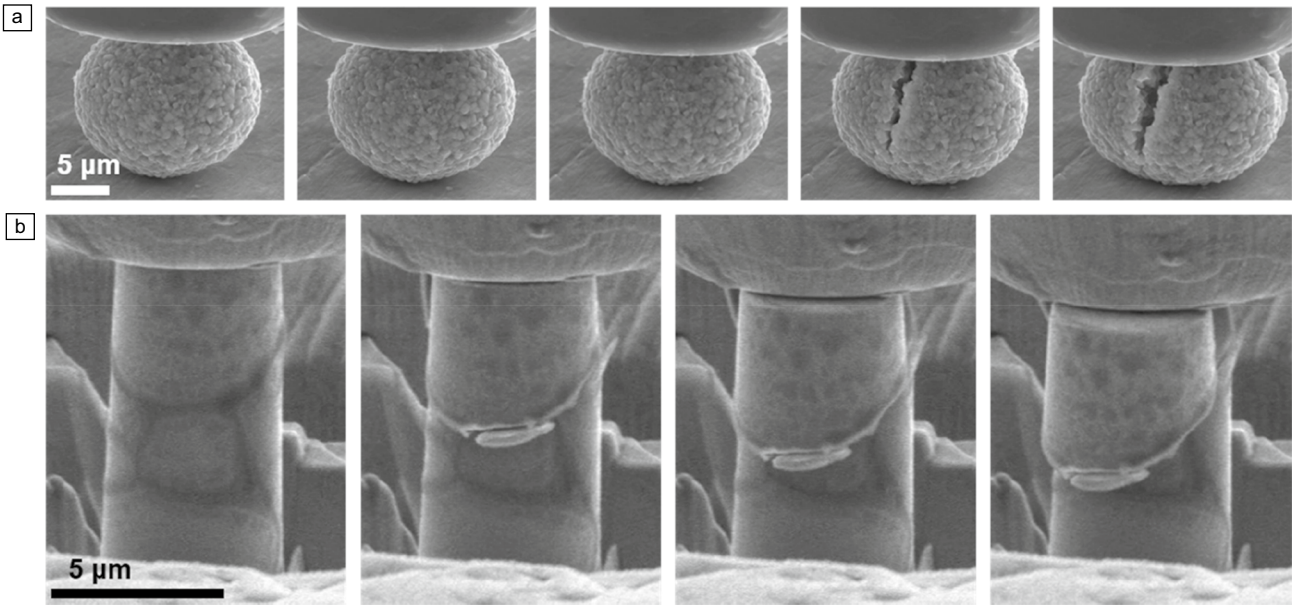


Figure 3. Examples of using *in situ* scanning electron microscope (SEM) micromechanical characterisation to investigate interfacial failure in non-structural materials. Real-time SEM images recorded during (a) compression of an agglomerated pristine (not electrochemically cycled) polycrystalline $Li(Ni_{0.8}Mn_{0.1}Co_{0.1})O_2$ (NMC811) particle and (b) compression of a sintered pristine polycrystalline NMC811 micropillar. The full videos are available in Videos S5 and S6. The load–displacement curve for the test in (a) is available in Figure S1c, and the engineering stress–strain curve for the test in (b) is available in Figure S1d. (a) The image is reproduced with permission from Reference 30.

to produce surface hydride rims, followed by annealing at 400°C for 5 h for hydrogen homogenization and slow cooling at 0.5°C/min to promote the formation of δ-hydride packets.[8]

The SiC/SiC CMCs with either BN or C interphases were manufactured using a preform of commercially available two-dimensional five-hardness satin fabric woven from Hi-Nicalon SiC fiber, supplied by NGS Advanced Fibres. The preform was coated with either BN or C via chemical vapor infiltration (CVI) and partially densified with CVI SiC. In the SiC/SiC CMC with BN interphases, the matrix was fully densified via slurry infiltration of SiC particles followed by melt infiltration with Si. The detailed manufacturing procedure was reported in Reference 20.

Single-crystalline and polycrystalline NMC811 particles were acquired commercially from Li-Fun Technology and Targray Technology International, respectively. The bulk NMC811 pellet was prepared through sintering the single-crystalline particles with 10% Li excess (Li_2CO_3). The particles were first pressed uniaxially into a pellet in a glovebox and then further pressed isostatically at 300 MPa prior to sintering in a Pt crucible at 1000°C for 10 h in static air. The detailed sintering process was reported in Reference 35.

All samples, apart from the NMC811 polycrystalline particles, were mechanically ground and polished prior to subsequent FIB milling and *in situ* testing, with a final polishing step using 0.04-µm colloidal silica and/or alumina.

All small-scale specimens, apart from the NMC811 polycrystalline particles, were fabricated through FIB milling on a Thermo Fisher Scientific (TFS) Helios 5 CX DualBeam microscope using a FIB acceleration voltage of 30 kV. *In situ* SEM micromechanical tests were all conducted using an Alemnis nanoindenter on a TFS Quanta 650 SEM. All indenter tips used were made of diamond and supplied commercially by Synton-MDP. *In situ* TEM experiments were conducted using a Hysitron™ PI 95 TEM PicoIndenter on a JEOL 2100F TEM operating at 200 kV. Details about sample/tip preparation and testing were reported in Reference 19. The TEM results presented in Figure 1b were acquired using a TFS Titan TEM at 200 kV acceleration voltage.

Acknowledgments

The Helios 5 and Hydra DualBeam microscopes are part of the cryo-EPS facility at Imperial College London, funded by Engineering and Physical Sciences Research Council (EPSRC, EP/V007661/1). The FEI Quanta 650 SEM was supported by the Shell AIMS UTC and housed in the Harvey Flower EM suite at Imperial College London. S.W. acknowledges Imperial College London for funding his Imperial College Research Fellowship. O.G.D., S.M., and H.N. acknowledge the Royal Society (ICA\R2\242079) for funding some of the tests highlighted in this article.

Author contributions

S.W., R.H., H.N., and O.G.D. performed the *in situ* SEM tests. S.M. and P.R. performed the *in situ* TEM tests. Z.S. prepared the NMC811 pellet. S.W. and O.G.D. wrote the original manuscript. S.W., S.M., H.N., Z.S., F.G., and O.G.D. reviewed the manuscript.

Funding

Engineering and Physical Sciences Research Council (GB)—EPSRC, EP/V007661/1. Imperial College Research Fellowship—N/A. Royal Society (GB)—ICA\R2\242079.

Data availability

Data will be made available on reasonable request.

Conflict of interest

On behalf of all authors, the corresponding author states that there is no conflict of interest.

Supplementary information

The online version contains supplementary material available at https://doi.org/10.1557/s43577-026-01234-4.

Open Access

This article is licensed under a Creative Commons Attribution 4.0 International License, which permits use, sharing, adaptation, distribution and reproduction in any medium or format, as long as you give appropriate credit to the original author(s) and the source, provide a link to the Creative Commons licence, and indicate if changes were made. The images or other third party material in this article are included in the article's Creative Commons licence, unless indicated otherwise in a credit line to the material. If material is not included in the article's Creative Commons licence and your intended use is not permitted by statutory regulation or exceeds the permitted use, you will need to obtain permission directly from the copyright holder. To view a copy of this licence, visit http://creativecommons.org/licenses/by/4.0/.

References

1. A.M. Minor, G. Dehm, *MRS Bull.* **44**(6), 438 (2019). https://doi.org/10.1557/mrs.2019.127
2. D. Kiener, A. Misra, *MRS Bull.* **49**(3), 214 (2024). https://doi.org/10.1557/s43577-023-00643-z
3. J.P. Niemela, B. Putz, G. Mata-Osoro, C. Guerra-Nunez, R.N. Widmer, N. Rohbeck, T.E. Edwards, M. Dobeli, K. Mackosz, A. Szkudlarek, Y. Kuzminykh, *ACS Appl. Nano Mater.* **5**(5), 6285 (2022). https://doi.org/10.1021/acsanm.2c00378
4. B. Putz, T.E. Edwards, E. Huszar, L. Pethö, P. Kreiml, M.J. Cordill, D. Thiaudiere, S. Chiroli, F. Zighem, D. Faurie, P.O. Renault, *Mater. Des.* (2023). https://doi.org/10.1016/j.matdes.2023.112081
5. C.R. Mayer, L.W. Yang, S.S. Singh, J. Llorca, J.M. Molina-Aldareguia, Y.L. Shen, N. Chawla, *Acta Mater.* **114**, 25 (2016). https://doi.org/10.1016/j.actamat.2016.05.018
6. S. Lotfian, M. Rodríguez, K.E. Yazzie, N. Chawla, J. Llorca, J.M. Molina-Aldareguía, *Acta Mater.* **61**(12), 4439 (2013). https://doi.org/10.1016/j.actamat.2013.04.013
7. S.G. Rao, R. Shu, S. Wang, R. Boyd, F. Giuliani, P. Eklund, *Mater. Des.* **224**, 111388 (2022). https://doi.org/10.1016/j.matdes.2022.111388
8. S. Wang, F. Giuliani, B.T. Ben, *Acta Mater.* **200**, 537 (2020). https://doi.org/10.1016/j.actamat.2020.09.038
9. A.T. Motta, L. Capolungo, L.Q. Chen, M.N. Cinbiz, M.R. Daymond, D.A. Koss, E. Lacroix, G. Pastore, P.C.A. Simon, M.R. Tonks, B.D. Wirth, *J. Nucl. Mater.* **518**, 440 (2019). https://doi.org/10.1016/j.jnucmat.2019.02.042
10. J.R. Rice, in *Proceedings of the 14th International Congress on Theoretical and Applied Mechanics*, vol. 1, ed. by W.T. Koiter (North-Holland Publishing Co., 1976), pp. 207
11. J.S. Weaver, N. Li, N.A. Mara, D.R. Jones, H. Cho, C.A. Bronkhorst, S.J. Fensin, G.T. Gray III , *Acta Mater.* **156**, 356 (2018). https://doi.org/10.1016/j.actamat.2018.06.046
12. S. Wang, S. Kalácska, X. Maeder, J. Michler, F. Giuliani, B.T. Ben, *Scr. Mater.* **173**, 101 (2019). https://doi.org/10.1016/j.scriptamat.2019.08.006
13. L. Gertlowski, T. Sedlatschek, O. Schenk, S. Müller, S. Benito, S. Weber, C. Broeckmann, *Mater. Lett.* (2026). https://doi.org/10.1016/j.matlet.2026.140880
14. G. Sernicola, T. Giovannini, P. Patel, J.R. Kermode, D.S. Balint, T.B. Britton, F. Giuliani, *Nat. Commun.* **8**(1), 1 (2017). https://doi.org/10.1038/s41467-017-00139-w
15. Z.L. Li, S. Wang, A. Li, J.O. Douglas, F. Bouville, O. Gavalda-Diaz, K.T. Marquardt, F. Giuliani *J. Eur. Ceram. Soc.* **46**(16), 118696 (2026). https://doi.org/10.1016/j.jeurceramsoc.2026.118696
16. Y. Zhang, M. Bartosik, S. Brinckmann, S. Lee, C. Kirchlechner, *Mater. Des.* (2023). https://doi.org/10.1016/j.matdes.2023.112188
17. J.W. Obreimoff, *Proc. R. Soc. Lond. A* **127**(805), 290 (1930). https://doi.org/10.1098/rspa.1930.0058
18. I. Issa, C. Gammer, S. Kolitsch, A. Hohenwarter, P.J. Imrich, R. Pippan, D. Kiener, *Mater. Today* **48**, 29 (2021). https://doi.org/10.1016/j.mattod.2021.03.009
19. O. Gavalda-Diaz, M. Emmanuel, A. Berenov, K. Marquardt, E. Saiz, F. Giuliani, *Proc. Natl. Acad. Sci.* **121**(43), 1 (2024). https://doi.org/10.1073/pnas.2408292121
20. O. Gavalda-Diaz, R. Manno, A. Melro, G. Allegri, S.R. Hallett, L. Vandeperre, E. Saiz, F. Giuliani, *Acta Mater.* (2021). https://doi.org/10.1016/j.actamat.2021.117125
21. M.Y. He, J.W. Hutchinson, *Int. J. Solids Struct.* **25**(9), 1053 (1989). https://doi.org/10.1016/0020-7683(89)90021-8
22. M. Rodríguez, J.M. Molina-Aldareguía, C. González, J. Llorca, *Compos. Sci. Technol.* **72**(15), 1924 (2012). https://doi.org/10.1016/j.compscitech.2012.08.011
23. C. Medinam, J.M. Molina-Aldareguía, C. González, M.F. Melendrez, P. Flores, J. Llorca, *J. Compos. Mater.* **50**(12), 1651 (2016). https://doi.org/10.1177/0021998315595115
24. D.B. Marshall, *J. Am. Ceram. Soc.* **67**(12), C259 (1984). https://doi.org/10.1111/j.1151-2916.1984.tb19690.x
25. E.B. Callaway, P.G. Christodoulou, F.W. Zok, *J. Mech. Phys. Solids* (2019). https://doi.org/10.1016/j.jmps.2019.07.016
26. C. Liang, J.W. Hutchinson, *Mech. Mater.* **14**, 207 (1993). https://doi.org/10.1016/0167-6636(93)90067-2
27. R.M.G. De Meyere, K. Song, L. Gale, S. Harris, I.M. Edmonds, T.J. Marrow, E. Saiz, F. Giuliani, D.E. Armstrong, O. Gavaldà-Diaz, *J. Mater. Res.* **36**(11), 2305 (2021). https://doi.org/10.1557/s43578-021-00153-1
28. S. Ghaffari, A. Makeev, G. Seon, D.P. Cole, D.J. Magagnosc, S. Bhowmick, *Mater. Des.* **193**, 108798 (2020). https://doi.org/10.1016/j.matdes.2020.108798
29. A. Leide, Á. Martinez-Pechero, G. Clark, C. Bearcroft, O. Gavalda-Diaz, S. Robertson, E. Demir, Y. Zayachuk, A. Widdowson, E. Tarleton, J. Wade-Zhu, *J. Eur. Ceram. Soc.* **45**(16), 117624 (2025). https://doi.org/10.1016/j.jeurceramsoc.2025.117624
30. A. Omirkhan, O. Gavalda-Diaz, S. Wang, I.E.L. Stephens, F. Giuliani, M.P. Ryan, *Energy Environ. Sci.* **18**(20), 9254 (2025). https://doi.org/10.1039/d5ee00976f
31. P.A. Rocco, A. Behvar, H.K. Bajaj, M. Haghshenas, M. Elahinia, *Shape Memory Superelast.* **12**(2), 284 (2026). https://doi.org/10.1007/s40830-026-00604-w
32. O. Glushko, A. Funk, V. Maier-Kiener, P. Kraker, M. Krautz, J. Eckert, A. Waske, *Acta Mater.* **165**, 40 (2019). https://doi.org/10.1016/j.actamat.2018.11.038
33. Z. Ning, G. Li, D.L.R. Melvin, Y. Chen, J. Bu, D. Spencer-Jolly, J. Liu, B. Hu, X. Gao, J. Perera, C. Gong, *Nature* **618**(7964), 287 (2023). https://doi.org/10.1038/s41586-023-05970-4
34. J. Kabel, T.E.J. Edwards, A. Sharma, J. Michler, P. Hosemann, *Carbon N Y.* **182**, 571 (2021). https://doi.org/10.1016/j.carbon.2021.06.045
35. S. Wang, Z. Shen, A. Omirkhan, O. Gavalda-diaz, M.P. Ryan, F. Giuliani, *J. Eur. Ceram. Soc.* **43**(16), 7553 (2023). https://doi.org/10.1016/j.jeurceramsoc.2023.08.021

Publisher's note Springer Nature remains neutral with regard to jurisdictional claims in published maps and institutional affiliations.